Experimental scaling of diffraction efficiency in laser-induced plasma gratings

M. M. Wang,[1,*,†] V. M. Perez-Ramirez,[2,*,‡] N. M. Fasano,[1] K. Ou,[2] S. Cao,[2] V. Dewan,[1] A. M. Giakas,[1] A. Morozov,[1] P. Michel,[3] M. R. Edwards,[2,§] and J. M. Mikhailova[1,‖]

[1]*Princeton University, Princeton, New Jersey, 08544 USA*
[2]*Stanford University, Stanford, California, 94305 USA*
[3]*Lawrence Livermore National Laboratory, Livermore, California, 94551 USA*

(Received 29 April 2026; accepted 29 September 2026; published 6 November 2026)

We demonstrate efficient diffraction of intense ultrashort laser pulses using optical-field-ionization-induced plasma-neutral gratings formed by spatially structured ionization of a neutral molecular gas in the interference field of two femtosecond pump pulses. The transient refractive index modulation of the plasma structure persists for at least 10 ps and is used to diffract intense femtosecond signal pulses into the first order of diffraction with an average efficiency of up to 35%. Plasma gratings are shown to provide stable diffraction at signal laser intensities greater than 10^{14} W/cm^2, exceeding the damage thresholds of conventional solid-state optics by more than two orders of magnitude, continuously for at least one hour at a 10-Hz repetition rate. The experimental diffraction efficiency scales with the grating aperture allowing for a larger millimeter-scale plasma optic, increases with the pump energy and electron density, and reaches a maximum at a specific grating length in agreement with the coupled-mode theory for periodic media. These results demonstrate the scalability, tunability, and high damage threshold of transmissive plasma-based photonic structures, opening new prospects for controlling multi-petawatt laser beams.

DOI: 10.1103/9q15-5b5w

I. INTRODUCTION

Ultraintense lasers reaching multi-petawatt peak powers are driving laser-based particle acceleration, high-energy photon sources, inertial fusion energy, and new regimes of nonlinear quantum electrodynamics [1–12]. However, further increases in peak laser power and intensity are constrained by laser-induced damage of solid-state optical components, which is difficult to mitigate due to the inherently stochastic spatial and temporal structure of high-power laser beams [13,14].

In contrast to conventional solid-state transmissive optics, where discrete quantum resonances of bound charges dominate the optical response and functionality, and the optical damage by pulsed lasers at high laser fluences is primarily due to ionization of the optical material, transient plasma-based optics make use of the collective response of already ionized free electrons created by laser-induced ionization in gases, liquids, or solids. Plasma structures can withstand higher intensities without degradation, allowing plasma-based optical components to be reduced in size from meters to millimeters for petawatt beams. The optical response of plasma electrons is intrinsically ultrafast and broadband [15], as it is largely determined by the plasma frequency, which depends on the free electron density and is therefore not restricted to specific wavelengths defined by quantum resonances [16]. By tailoring the electron density, plasma-based optical components can be engineered for high-power lasers across a wide spectral range from near-infrared petawatt [1–6,8] to mid-infrared multi-terawatt systems [17], ultrabroadband multicolor waveforms [7,18], and extreme-ultraviolet and x-ray sources [19–22]. In addition, the plasma-optic medium renews with each laser pulse; therefore, damage does not accumulate even at high repetition rates.

Recent advances in plasma optics include ultrafast optical switches for temporal contrast cleaning [23,24], relativistic plasma mirrors for high-energy photon sources [25–39] and for on-target diagnostics of intense ultrashort pulses [40], plasma waveplates [41,42], optical-field-ionization waveguides for laser wakefield acceleration [43–47], compressor gratings for chirped-pulse amplification [48–52], and holographic diffractive lenses [53,54], highlighting plasma optics as a rapidly developing area in high-power laser science and technology.

*These authors contributed equally to this work.
†Contact author: michelle.wang@princeton.edu
‡Contact author: vpr11@stanford.edu
§Contact author: mredwards@stanford.edu
‖Contact author: j.mikhailova@princeton.edu

Published by the American Physical Society under the terms of the Creative Commons Attribution 4.0 International license. Further distribution of this work must maintain attribution to the author(s) and the published article's title, journal citation, and DOI.

The formation of transient laser-induced plasma structures can be governed by either ponderomotive density modulation in ionized plasmas [49,55,56] or spatially varying ionization in a neutral gas [24,57–61]. Here, we focus on the latter mechanism, where spatially periodic optical field ionization creates a refractive index modulation between plasma and neutral gas regions. In our experiments, thick plasma-neutral gratings operate in the Bragg regime, where most of the incident energy is diffracted into the first order at the Bragg angle, defined by the criterion $\rho \gg 1$, with $\rho = \lambda^2/(\Lambda^2 n_0 n_1)$, where λ is the incident wavelength, Λ is the grating period, n_0 is the mean refractive index, and n_1 is the amplitude of the fundamental refractive index modulation for a sinusoidal grating [62].

The highest reported diffraction efficiency from femtosecond optical field ionization gratings in a neutral gas was approximately 19%, achieved with 100 fs ultraviolet (267 nm) pulses producing peak electron densities of approximately 10^{19} cm^{-3} in air [58]. Plasma-neutral gratings have also been generated through collisional ionization with longer picosecond pulses, yielding average efficiencies up to 36% using 1064 nm, 120 ps, < 250 mJ pump pulses that produced plasma densities approaching 1.5×10^{19} cm^{-3} in an argon-cluster jet to diffract a 3.9 μm signal beam [63]. Higher diffraction efficiency is expected for longer signal wavelengths due to the inverse-square scaling of the critical plasma density with the signal beam wavelength. The plasma refractive index is $n_{\text{plasma}} = \sqrt{1 - N_e/N_c}$, where N_e is the electron density and $N_c = \epsilon_0 m_e \omega_0^2/e^2 \propto 1/\lambda_0^2$ is the critical plasma density. The resulting increase in refractive index contrast between plasma and neutral regions, combined with an optimal grating length, can enhance the diffraction efficiency for longer signal wavelengths.

Here, we demonstrate high diffraction efficiency of field-ionized plasma-neutral gratings over a range of grating parameters. Using near-IR (800 nm), 29 fs pump pulses with mJ-level energies, we generate ionization gratings with peak electron densities of only approximately 4×10^{17} cm^{-3}, which is more than an order of magnitude lower than in previous studies [58,63], while achieving a maximum average diffraction efficiency of 35%. We systematically investigate how the diffraction efficiency scales with key grating parameters including transverse size, length, and electron density. Millimeter-scale gratings are shown to sustain diffracted signal intensities up to 2.4×10^{14} W/cm^2, demonstrating potential for scalable beam control in multi-petawatt laser systems.

II. EXPERIMENTAL SETUP

A plasma-neutral grating is generated by spatially and temporally overlapping two femtosecond pump beams in a neutral gas. A schematic of the experimental setup at Princeton is shown in Fig. 1(a). The pump and signal

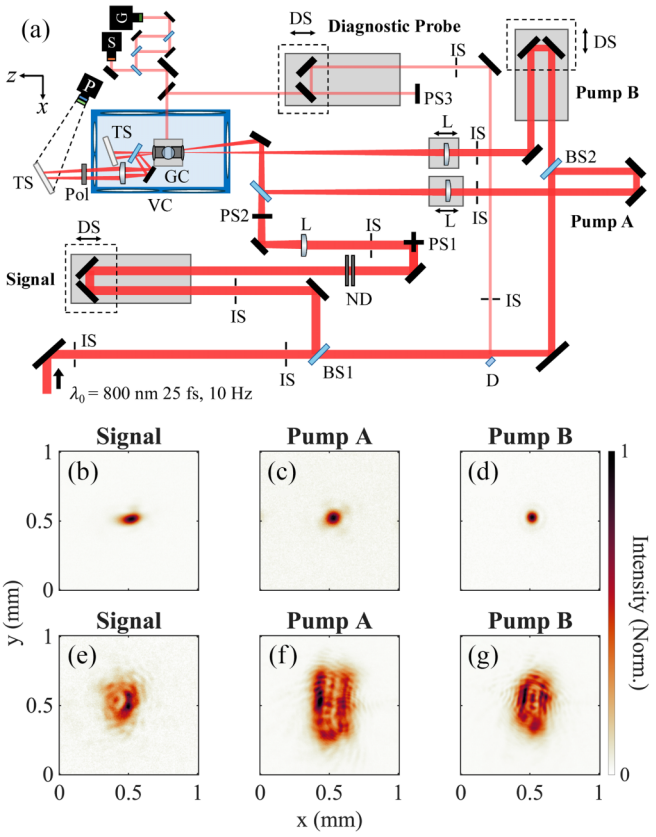


FIG. 1. (a) Schematic of the plasma grating experimental setup. Key components: iris (IS), beamsplitter (BS), D-shaped pick-off mirror for a plasma diagnostic probe (D), automated beam shutter (AS), motorized delay stage (DS), neutral density filter (ND), periscope (PS1, PS2, PS3), lens (L), gas cell (GC), vacuum chamber (VC), linear polarizer (Pol), and Teflon scattering screen (TS). Camera P images the pump and signal beam scattering from the Teflon screen to measure the diffraction efficiency, camera S is used for plasma grating shadowgraphy, and camera G for interferometric measurements of the electron density. (b–g) Beam profiles at the gas cell: small-aperture grating—(b) signal, (c) pump A, (d) pump B; large-aperture grating—(e) signal, (f) pump A, and (g) pump B.

beams are obtained from a 20-TW Ti:Sapphire laser (Princeton Pulsar 20 TW, Amplitude; central wavelength $\lambda_0 = 800$ nm, pulse duration $\tau = 25$ fs, 10-Hz repetition rate). Two s-polarized pump beams (pump A and pump B) propagate in the xz plane and intersect at a full crossing angle of $\theta_p = 3°$ at the center of a CO_2 filled gas cell inside a vacuum chamber, forming a grating with period $\Lambda = 15.3$ μm. The pump pulse duration was measured after compression and used to estimate the pulse durations of pumps A and B at the gas cell, taking into account the dispersion introduced by transmissive optics along the pump-beam paths. Optical pulse dispersion was fine tuned by a programmable dispersive filter (acousto-optic modulator Dazzler, Fastlite). This yielded an average FWHM intensity duration of $\tau_p = 29 \pm 4$ fs for pumps A and B at the gas cell. Laser input and output apertures in the cell are

formed by ablating 50-μm-thick steel foils mounted on the gas cell walls, while maintaining a residual CO_2 pressure of 1–6 mbar. After the grating is formed, a high-power signal beam is focused onto the grating at the Bragg angle of incidence:

$$\theta_B = \arcsin\left(\frac{\lambda_0}{2\Lambda}\right), \tag{1}$$

where $\Lambda = \lambda_1/(2\sin(\theta_p/2))$ is the plasma grating period, λ_0 is the central wavelength of the signal beam, and λ_1 is the central wavelength of the pumps. For $\lambda_0 = \lambda_1 = 800$ nm, the Bragg angle is $\theta_B = 1.5°$, equal to half the pump crossing angle. The signal beam is p-polarized to avoid interference with the pump beams. The signal duration at the gas cell is $\tau_s = 41 \pm 8$ fs, derived from pulse duration measurements at the compressor taking into account the dispersion in transmissive optics. Signal and pump-beam profiles at the gas cell are shown in Figs. 1(b)–1(d) for the small-aperture grating and Figs. 1(e)–1(g) for the large-aperture grating. After propagation through the gas cell, the undiffracted signal, diffracted signal, and residual pump beams are incident on a Teflon scattering screen (TS), which is imaged with a high dynamic range camera P [Fig. 1(a)]. Beam profiles recorded with camera P are used to determine the absolute diffraction efficiency η, defined as the ratio of the diffracted signal counts to the total transmitted signal counts through the gas cell. Absorption of the signal beam in the grating is negligible at studied laser intensities and does not significantly affect the transmission. The diffraction efficiency of the signal beam is measured as a function of the grating dimensions, pump-beam energy, electron density N_e, and signal beam energy.

A. Beam geometry for small- and large-aperture gratings

Experimental configurations used for grating scalability studies are shown in Fig. 2. Two plasma gratings of different transverse apertures D were generated and characterized: (1) a small-aperture grating [Figs. 2(a) and 2(c)] with $D =$ 23 μm generated at the pump focal plane ($z_{\mathrm{f,pumps}} = 0$), and (2) a large-aperture grating [Figs. 2(b) and 2(d)] with $D =$ 98 μm (4.3 × larger) generated 2 cm before the pump focus ($z_{\mathrm{f,pumps}} = 2$ cm), beyond the pump Rayleigh length. The aperture D was defined as the distance between sharp edges of the transverse electron density profiles, shown by the gray shaded regions in Figs. 3(c) and 3(d). The parameter $z_{\mathrm{f,pumps}}$ in Fig. 2 denotes the position of the pump-beam focus relative to the center of the gas cell ($z = 0$).

For the small-aperture configuration [Fig. 2(a)], pump A and pump B propagate in the $x - z$ plane and intersect at their waists at $z_{f,\mathrm{pumps}} = 0$ with a residual CO_2 pressure of approximately 6.0 mbar. The signal beam (15-mm diameter before focusing) is collinear with pump A and diffracts in the xz plane. After the gas cell, the beams are incident onto a Teflon scattering screen (TS) imaged by camera P [Fig. 1(a)]. For the small-aperture grating setup with in-plane diffraction, a linear polarizer labeled Pol in Fig. 1(a) was placed before the Teflon scattering screen to filter out the residual pump beams since the signal beam was not spatially separated in this configuration. The polarizer was omitted in the large-aperture configuration because the diffracted signal beam was spatially separated as a result of the signal beam being directed out of the horizontal xz plane. The undiffracted and diffracted signal beam profiles on TS are shown in Fig. 2(a), with the diffracted beam highlighted by the black box after subtraction of the residual pump-beam background.

For the large-aperture configuration [Fig. 2(b)], the pump beams intersect 2 cm upstream of their foci ($z_{\mathrm{f,pumps}} = 2$ cm). The signal beam is directed out of the xz plane by the first periscope [PS1 in Fig. 1(a)] and aligned vertically co-planar with Pump A in the yz plane with azimuthal angle θ_B. It is incident with a downward angle of approximately 2° introduced by a second periscope [PS2 in Fig. 1(a)] to spatially separate the undiffracted and diffracted signal beams after interaction with the grating. The residual CO_2 pressure was maintained at approximately 1.4 mbar. This lower pressure was selected to minimize laser filamentation and supercontinuum generation at higher beam energies while maintaining electron densities comparable to those obtained with the small-aperature configuration. The diffracted signal beam is outlined by a black box on the Teflon scattering screen behind the gas cell in Fig. 2(b). The signal beam diameter is increased to 19 mm before focusing to enable higher signal energies for damage-threshold measurements. The pump interference pattern at $z = 0$ is recorded on a camera placed directly at the pumps intersection at alignment power and is shown in the left corner of Figs. 2(a) and 2(b). A weaker diagnostic probe beam propagating along the y axis transversely through the plasma grating is used for shadowgraphy using camera S [Fig. 1(a)], and interferometric electron density measurements via plasma-induced phase shifts using a folded Mach-Zehnder interferometer [64] with the grating located outside of the interferometer arms. Plasma grating shadowgraphs and top-view schematics of the pump beam crossing inside the gas cell for the two configurations are shown in Figs. 2(c) and 2(d). Fourier transform analysis of the interferogram recorded by camera G [Fig. 1(a)] is used to extract the electron density profiles of the grating, shown in Fig. 3.

III. SCALABILITY AND PARAMETER DEPENDENCE OF DIFFRACTION EFFICIENCY

An ideal Bragg grating can reach 100% diffraction efficiency [62]. However, for focused ultrashort-pulse beams, the spectral bandwidth of the signal and its angular divergence reduce the diffraction efficiency. The resulting

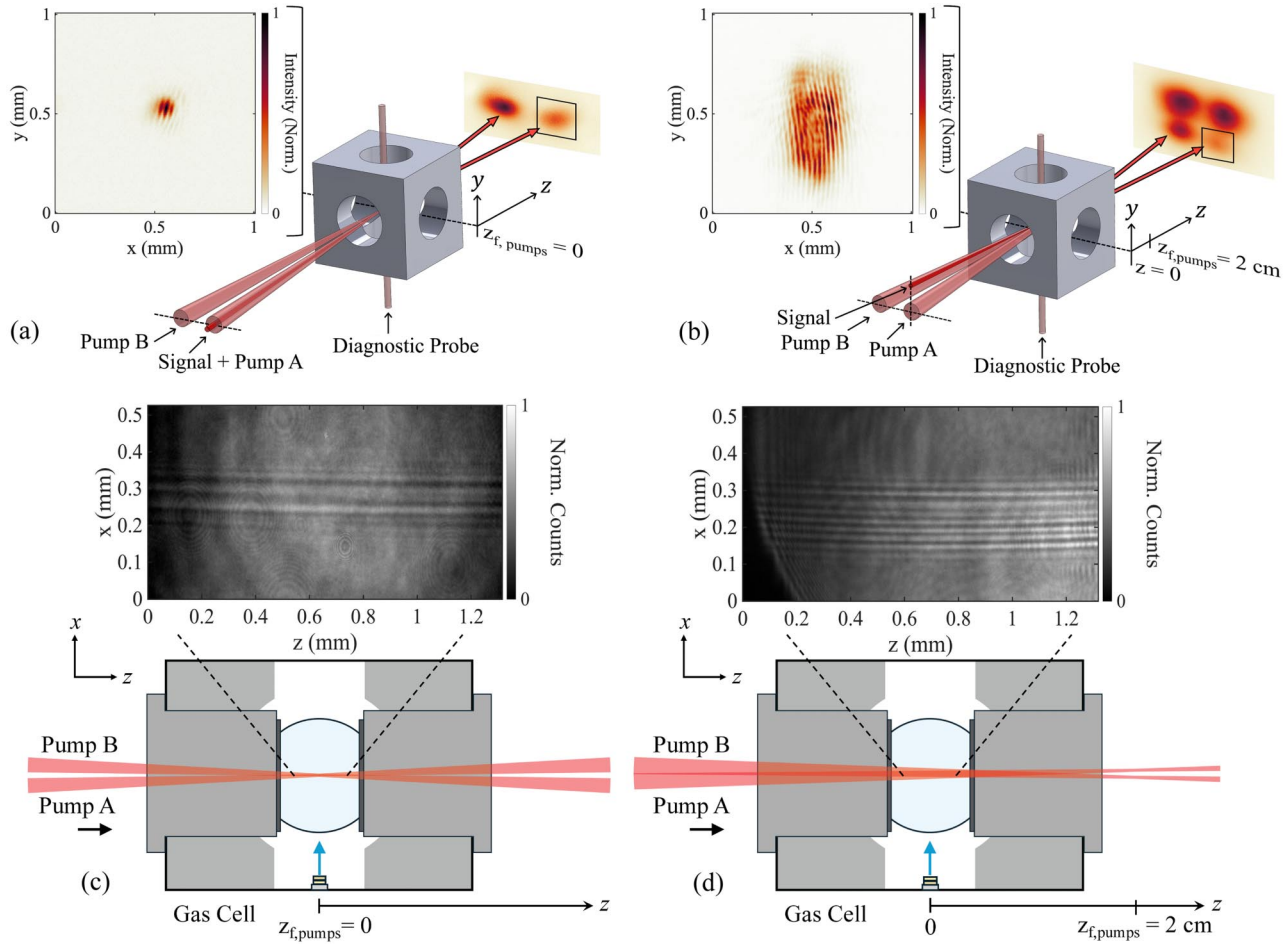


FIG. 2. (a) The beam geometry inside the gas cell is shown for the small-aperture grating with pump beams focused at the center of the gas cell at $z_{f,pumps} = 0$ and the signal beam co-linear with pump A. The transverse interference pattern is shown to the left of the GC. The image of the Teflon scattering screen after the gas cell is shown after subtracting out the residual pump beams with the diffracted beam outlined by the black square. (b) The beam geometry for the large-aperture grating with pump beams focused at $z_{f,pumps} = 2$ cm after the center of the gas cell with the signal beam directly above pump A angled downward onto the grating. The diffracted signal beam is outlined by the black square. The red arrows indicate the beams' propagation after the gas cell (optics after the gas cell are not depicted). The interference pattern of the pump beams is shown in both (a),(b) at $z = 0$. The top-down view of the pump beams crossing inside the gas cell is shown for the (c) small- and (d) large-aperture grating. Blue arrow denotes direction of gas flow from nozzle. Insets above (c),(d) show corresponding shadowgraphs.

diffraction efficiency (%) can be described using coupled-mode theory [65] as

$$\eta(L) = \frac{100\% \times \kappa^2}{\kappa^2 + (\frac{\Delta\alpha}{2})^2} \sin^2\left(\kappa L\left[1 + \left(\frac{\Delta\alpha}{2\kappa}\right)^2\right]^{\frac{1}{2}}\right), \quad (2)$$

where $\kappa = \pi n_1/(\lambda \cos\theta_B)$ and $\Delta\alpha = 2\pi n_0(\cos\theta_2 - \cos\theta_1)/\lambda$. Here, θ_1 and θ_2 are the signal incidence and diffraction angles, λ is the wavelength of a spectral component within the signal's bandwidth, n_0 is the average refractive index ($n_0 \approx 1$), L is the grating length, $n_1 = n_0 - n_{\text{plasma}}$ is the amplitude of the fundamental Fourier component of the refractive index modulation, and κL is the grating coupling strength [65]. Single-shot Mach-Zehnder interferometry measurements yield peak electron densities between 1×10^{17} and 5×10^{17} cm^{-3}. Single-shot electron density profiles reconstructed from interferometric phase maps are shown for the small- and large-aperture gratings in Figs. 3(a) and 3(b), with corresponding vertical lineouts in Figs. 3(c) and 3(d), demonstrating well-defined periodic grating structures with apertures $D = 23$ μm and $D = 98$ μm.

A. Dependence of diffraction efficiency on grating length

The diffraction efficiency η was first characterized as a function of the grating length L, controlled by varying the distance between the walls of the gas cell. The measured efficiencies for the small-aperture grating are shown in Fig. 4(a) (gray circles denote single shots, red circles

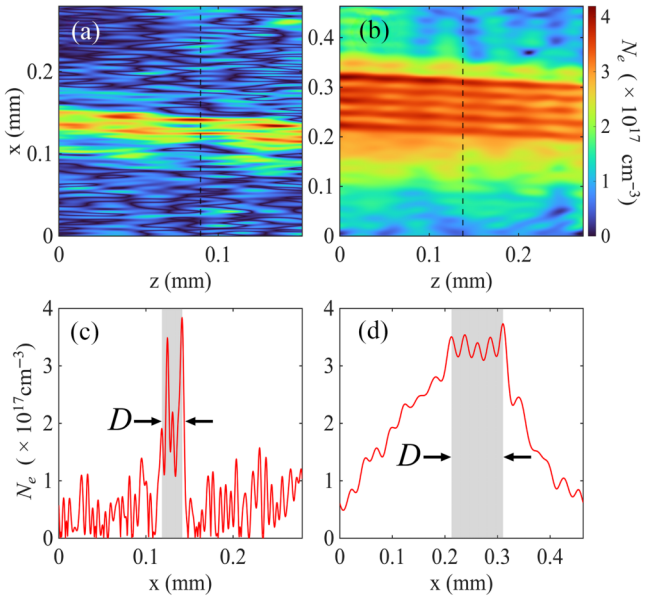


FIG. 3. Spatial distributions of electron density in the (a) small- and (b) large-aperture plasma grating retrieved by two-dimensional Fourier transform analysis of the plasma-induced phase shift in the interferogram obtained with the folded Mach-Zehnder interferometer. Lineouts of the electron density at $z = 0.09$ mm (small-aperture) and $z = 0.14$ mm (large-aperture) are shown in (c),(d), respectively. The gray shaded regions indicate the grating apertures, $D = 23$ μm and $D = 98$ μm.

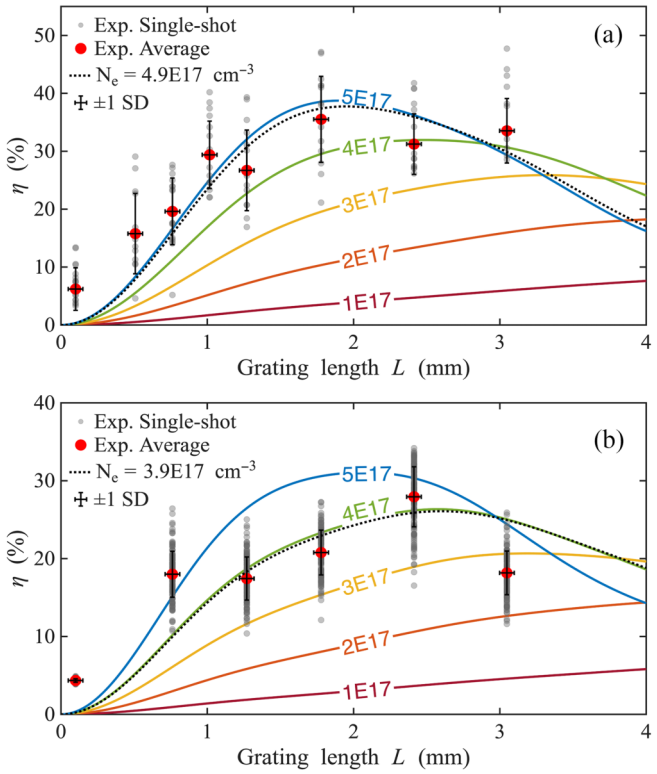


FIG. 4. Experimental (circles) and theoretical (lines) diffraction efficiency versus grating length for the (a) small- and (b) large-aperture gratings. Red circles show measured average efficiency with black error bars indicating the standard deviation (SD), and gray circles show single-shot efficiencies. The dotted black line is a best-fit obtained by numerical integration of Eq. (2), including Bragg condition mismatch from angular and spectral bandwidths, with the electron density as a free parameter. The fit yields average electron densities of 4.9×10^{17} and 3.9×10^{17} cm^{-3} for the small- and large-aperture gratings, respectively.

denote averages), reaching a maximum average efficiency of 35% and a maximum single-shot efficiency of 48% at $L = 1.78$ mm. For the large-aperture grating, [Fig. 4(b)] the maximum average efficiency is 28% and the maximum single-shot efficiency is 34% at $L = 2.41$ mm. In both configurations, the efficiency peaks at an optimal grating length and decreases for both shorter and longer gratings.

The solid lines in Figs. 4(a) and 4(b) show theoretical efficiencies obtained by numerically integrating Eq. (2) for plasma densities between 1×10^{17} and 5×10^{17} cm^{-3}, accounting for deviations from the ideal Bragg condition due to the signal beam divergence ($\Delta\theta_1 = \pm 0.43°$ and $\pm 0.54°$ for the small- and large-aperture gratings, respectively) and pulse spectral bandwidth $\Delta\lambda = 0.1\lambda_0 = 80$ nm. The dotted lines represent fits of Eq. (2) to the experimental data with the electron density N_e as a free parameter, yielding 4.9×10^{17} and 3.9×10^{17} cm^{-3} for the small- and large-aperture gratings, respectively.

The lower efficiency of the large-aperture grating can be attributed to several factors. First, the larger diameter of the signal beam (19 vs 15 mm), used to increase the signal energy for damage-threshold measurements of the large-aperture configuration, increases the angular spread at focus (f-number $f/53$ vs $f/67$ for $f = 1000$ mm lens), leading to greater deviation from the Bragg condition. Second, transverse nonuniformities in the spatial profiles of the pump beams, which, for the large-aperture grating, intersect in their near-field regions before their waists, introduce spatial variations in the interference pattern. To quantify this effect, we estimate the transverse variation in the peak electron density at the interference fringes from the measured pump-beam interference intensity profile. These variations produce localized regions of higher and lower electron density in the fringes across the grating aperture, resulting in a spatially varying grating strength and phase-matching condition. For example, for a propagation length of $L = 3$ mm, a uniform grating with a consistent peak electron density at the interference fringes of 4.2×10^{17} cm^{-3} yields a calculated diffraction efficiency of 26%, whereas a grating with consistent peak electron density of 1.6×10^{17} cm^{-3} yields an efficiency of 9%. Both electron density values were obtained from the estimated peak fringe electron densities previously mentioned and is shown in Appendix. Thus, the transverse variation in peak electron density across the large-aperture configuration can locally reduce the grating strength,

contributing to the lower measured diffraction efficiency. Lastly, the average peak plasma density is lower for the large-aperture grating, further reducing the overall grating strength.

B. Dependence of diffraction efficiency on pump intensity and electron density

The dependence of the diffraction efficiency η on the pump intensity and corresponding electron density N_e, measured with interferometry, was investigated by varying the pump energy for the large-aperture grating. The pump intensity is defined as the average intensity of the interference pattern formed by the two pump beams. The individual pump intensities are estimated as $I_{A,B} = \sqrt{4\ln 2/\pi}\, W_{A,B}/(A_{A,B} \cdot \tau_p)$, where $W_{A,B}$ and $A_{A,B}$ are the pulse energies and beam cross-sectional areas, respectively. The spatial profiles and cross-sectional areas of the pump beams and their interference pattern at the position of the plasma grating were estimated from low-energy beam profiles recorded directly on a CCD, as shown in Figs. 1(f), 1(g), and 2(b). Figure 5(a) shows monotonic increase of diffraction efficiency and electron density with increasing pump intensity, and Fig. 5(b) shows the measured diffraction efficiency as a function of the measured electron density along with the calculated efficiency (dotted line) using Eq. (2) for a grating length $L = 2.67$ mm, taking into account the Bragg condition mismatch due to finite spectral bandwidth, $\Delta\lambda = 80$ nm, and angular divergence ($\Delta\theta_1 = \pm 0.54°$ about $\theta_B = 1.5°$), corresponding to a signal beam of 19 mm diameter incident on an $f = 1000$ mm lens. These results indicate that higher diffraction efficiencies can be achieved at higher electron densities, corresponding to larger refractive index modulation amplitudes.

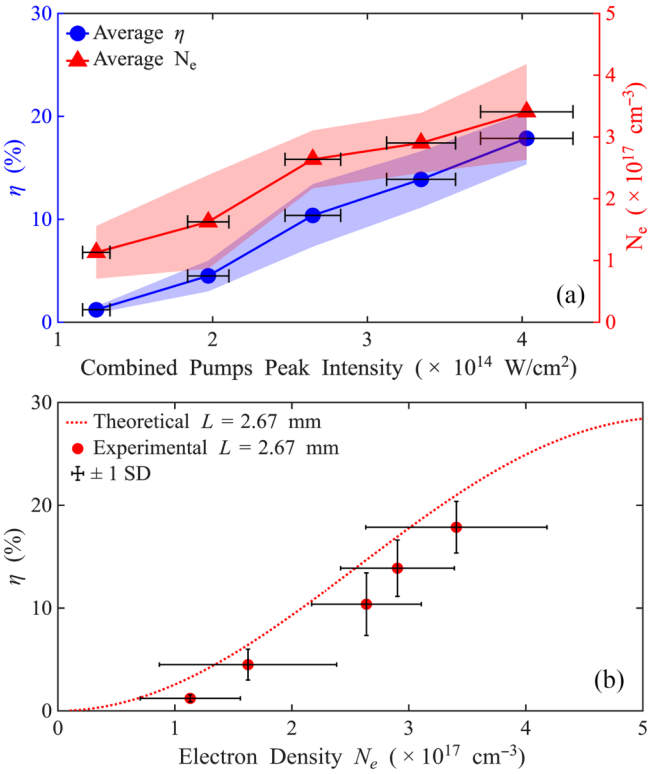


FIG. 5. (a) Average diffraction efficiency (blue circles) and electron density (red triangles) as a function of pump intensity for grating length $L = 2.67$ mm. Blue and red shaded regions indicate the standard deviation (SD) over 400 single shots (efficiency) and 100 single shots (electron density), respectively. Horizontal error bars show the standard deviation of the average intensity of the interference pattern formed by the two pump beams. (b) Average diffraction efficiency as a function of electron density, controlled by varying the pump energy. Red circles show the average experimental η for $L = 2.67$ mm with error bars corresponding to one standard deviation over 100 single shots. The red dotted line shows the theoretical prediction calculated using $\Delta\lambda = 80$ nm and $\Delta\theta_1 = \pm 0.54°$ in Eq. (2).

C. Intensity tolerance of plasma gratings

To study the signal-intensity tolerance of the plasma-neutral grating, the signal beam energy was varied from 0.92 to 8.5 mJ using neutral density filters (ND in Fig. 1). The signal intensity is estimated as $I = \sqrt{4\ln 2/\pi}\, W_s/(A_s\tau_s)$, where W_s is the signal beam energy and A_s is the cross-sectional area of the signal beam. The spatial profile [Fig. 1(e)] and cross-sectional area of the signal beam were recorded directly on a CCD placed at the position of the plasma grating with an attenuated signal beam. The peak signal intensities at the plasma grating varied from approximately 3.2×10^{13} to 2.4×10^{14} W/cm^2 (Fig. 6). Across

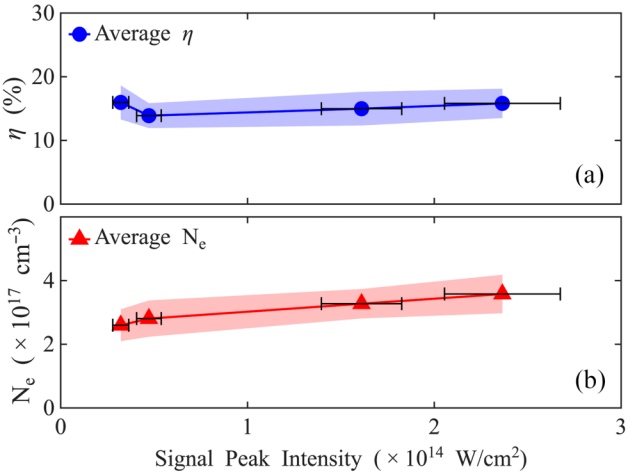


FIG. 6. (a) Diffraction efficiency and (b) electron density dependence on signal beam intensity for grating length $L = 2.67$ mm averaged over 100 single shots. The blue circles show average diffraction efficiency, and red triangles show average electron density. Shaded area indicates the standard deviation over 100 single shots, and horizontal error bars indicate the standard deviation of signal intensity.

this range of signal intensities, the diffraction efficiency decreased by less than 1% [Fig. 6(a)], indicating no measurable degradation of the grating on the interaction timescale. The average peak electron density increased by 38%, from 2.6×10^{17} to 3.6×10^{17} cm^{-3} [Fig. 6(b)]. These results indicate weak signal-induced ionization without measurable degradation of grating performance. Long-term stability was further evaluated by continuous operation for 1 hour at 10-Hz pulse repetition rate, during which the diffraction efficiency fluctuated by 2% (standard deviation) with no systematic decrease.

IV. PLASMA GRATING LIFETIMES

The lifetime of the ionization-induced refractive index modulation sets the operational time window of plasma-neutral gratings for high-intensity and multi-petawatt laser applications. The evolution and lifetime of the transient plasma-neutral grating were characterized by scanning a temporal delay of the signal pulse relative to the pump pulses, denoted by Δt_{signal}, and monitoring the diffraction efficiency of the signal. In molecular gases, such as CO_2 used in this work, both collisional electron recombination and diffusion contribute to the degradation of the grating structure [57,59,66]. In collisional electron recombination, the electron recombines with the parent carbon dioxide ion with the assistance of a second CO_2 molecule, which acts as a third body to carry away excess energy and momentum: $e^- + CO_2^+ + CO_2 \rightarrow CO_2 + CO_2$ [57]. The plasma can also decay through ambipolar diffusion, in which the higher mobility of free electrons causes them to diffuse from the ionized regions toward the surrounding neutral regions due to the thermal pressure [59]. This initial charge separation generates an electric field that couples the electron and ion motion, driving the heavier ions in the same direction. Consequently, both electrons and ions diffuse away from the initially ionized regions toward the adjacent neutral regions, progressively smoothing the spatial electron density modulation. As this diffusion continues, the amplitude of the density modulation decreases until the plasma grating is effectively washed out [59]. The plasma structure decay also depends on the grating period. Smaller periods accelerate washout of the refractive index modulation, and the grating lifetime becomes shorter than the characteristic electron recombination time and is therefore primarily diffusion-limited [66].

In this work, the plasma grating structure remained stable without significant degradation for tens of picoseconds in both small- and large-aperture configurations, as is demonstrated by the pump-signal delay scans of the diffraction efficiency shown in Figs. 7(a) and 7(b), where gray circles denote 100 single-shot measurements at each delay and red circles show the averages. Zero delay corresponds to the maximum temporal overlap between the signal and pump pulses. Positive signal delay indicates

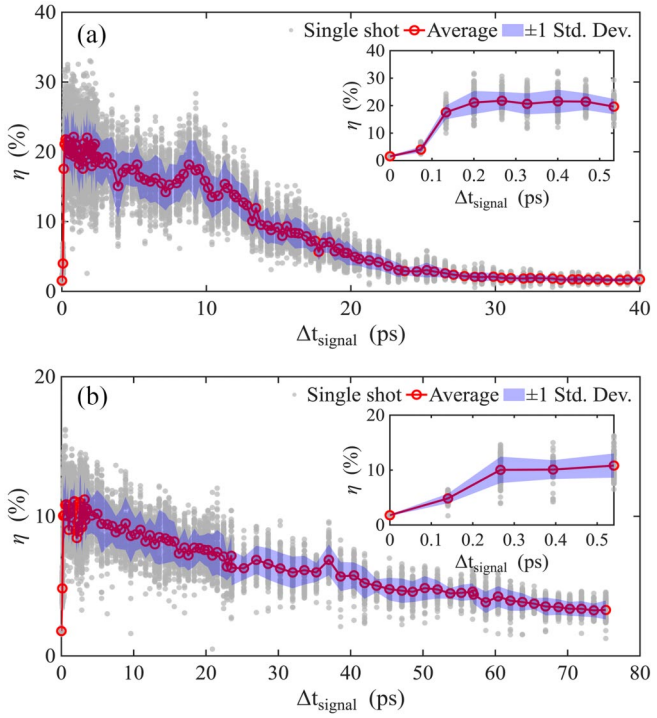


FIG. 7. Diffraction efficiency as a function of the pump-signal delay Δt_{signal} for the (a) small- and (b) large-aperture grating. Gray circles show each of the 100 single shots taken at each signal delay, and red circles show the average of each burst of 100 individual shots. The shaded blue region indicates one standard deviation. Maximum single-shot diffraction efficiency for the small- and large-aperture gratings is 33% and 16%, respectively. Inset plots show grating switch-on behavior immediately after $\Delta t_{signal} = 0$.

the signal pulse arriving later in time relative to the pump pulses. Exponential fits to the data yield $1/e$ lifetimes of $\tau_{1/e} = 17$ ps and $\tau_{1/e} = 68$ ps for the small- and large-aperture gratings, respectively. The longer lifetime and slower switch-on time of the large-aperture grating may arise from spatial-temporal coupling where the interference, produced by the pump beams in their near-fields, has a larger effective interaction region. In contrast, the interference pattern for the small-aperture grating is more tightly confined in space and time, resulting in faster switch-on and decay outside the temporal overlap. The observed picosecond-scale lifetimes of the refractive index modulation in the plasma grating structures support efficient diffraction of ultrashort pulses.

V. CONCLUSION

To summarize, we used the basic physics of strong-field light-matter interaction to create reconfigurable plasma-based photonic structures in a neutral gas for controllable diffraction of high-intensity ultrashort laser pulses and characterized their performance and scalability. The diffraction efficiency of the plasma gratings was measured as

a function of grating dimensions, pump laser intensity, electron density, and diffracted signal intensity. Two configurations were under study: a small-aperture grating, formed by the focused pump beams crossing at their waists, achieving up to 35% average diffraction efficiency, and a larger aperture grating formed by the pump beams crossing before their waists, capable of diffracting higher-energy signal pulses with average efficiencies up to 28%. For both configurations, the diffraction efficiency was optimal at a specific grating length in agreement with the coupled-mode theory for Bragg diffraction. The grating lifetime, measured by scanning the pump-signal delay, is on the order of 10 ps, which is long enough to control ultrashort pulses. We observed stable continuous operation of plasma gratings at signal laser intensities of up to $2.4 \times 10^{14}\,\mathrm{W/cm^2}$ (fluence $\approx 10.3\,J/\mathrm{cm^2}$), substantially exceeding the damage threshold of solid-state optics. The efficiency and stability of large-aperture gratings demonstrate the scalability of plasma gratings for applications requiring larger plasma optic sizes such as a diffractive plasma lens or plasma grating for higher-energy lasers. Further improvements in diffraction efficiency can be achieved through laser beam pointing stabilization, correction of pump wavefront aberrations using adaptive optics, reduction of Bragg condition mismatch, and optimization of the grating coupling strength κL. These results demonstrate the feasibility of transient plasma photonic structures as scalable optical components for integration into multi-petawatt laser facilities. In particular, their millimeter-scale size, high damage tolerance, regenerative operation, and ultrafast switch-on dynamics make them promising candidates for final-stage or near-final-stage beam manipulation including plasma-based compressor gratings, optical gating for temporal contrast cleaning, and robust beam steering. The use of a gaseous, transient medium further allows the optical structure to be regenerated on each shot, offering a potential pathway toward high-intensity optical components that can operate beyond the limitations of conventional solid-state optics.

ACKNOWLEDGMENTS

This work was partially supported by the U.S. Department of Energy under Grants No. DE-SC0025497 and No. DE-SC0025577, the U.S. National Science Foundation under Grants No. PHY-2206711, No. PHY-2308641, No. PHY-2512131, and No. PHY-2541940, the National Science Foundation Graduate Research Fellowship under Grant No. DGE-2146755 (V. M. P.-R.), the National Nuclear Security Administration under Grant No. DE-NA0004130, and the Gordon and Betty Moore Foundation Grant DOI 10.37807/gbmf12255. Lawrence Livermore National Laboratory is operated by Lawrence Livermore National Security, LLC, for the U.S. Department of Energy, National Nuclear Security Administration under Contract No. DE-AC52-07NA27344.

DATA AVAILABILITY

The experimental and theoretical data supporting the findings of this study are openly available at [68].

APPENDIX: EFFECT OF ELECTRON DENSITY NONUNIFORMITIES ON DIFFRACTION EFFICIENCY FOR THE LARGE-APERTURE GRATING

Since the large-aperture grating is formed in the near field of the pumps, spatial nonuniformities in the pump intensity can lead to transverse variations in the electron density and consequently affect the diffraction efficiency. Although an exact experimental determination of the transverse electron density uniformity is not possible because the interferometric measurement provides an integrated electron density signal and the transverse pump-beam interference pattern was characterized at reduced alignment power, we perform an approximate quantitative analysis to estimate the effect of transverse electron density nonuniformity on the diffraction efficiency of the large-aperture grating. Specifically, we use a simplified ADK tunneling ionization model [67] for single ionization of CO_2 to obtain an approximate two-dimensional transverse electron density distribution from the measured pump-beam interference intensity distribution shown in Fig. 2(b). The local ionization rate is integrated over the pump pulse duration to obtain the corresponding ionization probability and electron density. We then extract the electron density maxima from a transverse lineout of the calculated density distribution along the center of the interference pattern for a signal beam incident at the center of the grating. The two-dimensional spatial distribution of the estimated electron density is shown in Fig. 8(a), and the transverse lineout is shown in Fig. 8(b). The lineout contains 9 distinct electron density peaks with $N_e > 1 \times 10^{17}\ \mathrm{cm^{-3}}$. Each of these 9 peak electron densities was used to calculate the diffraction efficiency with the coupled-wave model while maintaining the experimentally relevant grating period, spectral and angular bandwidths, and propagation length. This procedure provides an estimate of the diffraction efficiency associated with each fringe as if it was part of an otherwise ideal grating with uniform electron density across the transverse aperture. A signal beam propagating through the nonuniform grating would experience a combination of these electron densities, and its diffraction efficiency would therefore reflect their cumulative effect. The corresponding diffraction efficiencies calculated for the 9 peak electron densities, along with that for the average experimental electron density, are shown in Fig. 9. Each

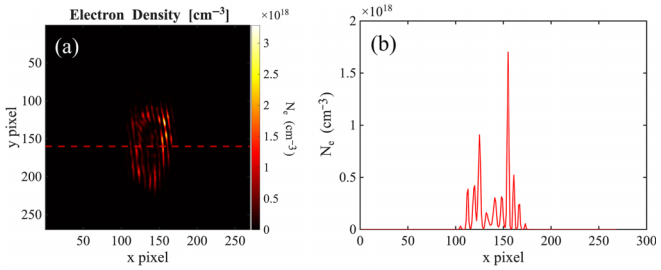


FIG. 8. (a) Two-dimensional spatial distribution of the estimated electron density, with the transverse lineout indicated by the red dashed line. (b) Electron density profile obtained from the transverse lineout of the pump-beam interference pattern. The variation in the peak electron density among individual grating fringes is used to estimate the resulting variation in diffraction efficiency.

electron density peak in the lineout represents an individual plasma grating fringe.

The calculation shows that transverse density variations can substantially reduce the diffraction efficiency over the full grating length. Localized regions with relatively high electron density can produce high diffraction efficiency over short propagation distances, but subsequently lose phase matching as the signal beam propagates through the grating, causing the efficiency to decrease. For example, for a grating length of $L = 3$ mm, an ideal grating with a uniform electron density of 4.2×10^{17} cm^{-3} yields a calculated diffraction efficiency of 26%, whereas an electron density of 1.6×10^{17} cm^{-3} yields an efficiency of 9%. The range of densities obtained from the transverse lineout therefore corresponds to substantial variations in the expected diffraction efficiency. The net effect of the nonuniform fringe electron densities is expected to produce a lower diffraction efficiency for some grating lengths than that predicted for an ideal grating with a uniform electron density. This estimated reduction is consistent with the experimental results in Fig. 4(b), where the measured average diffraction efficiency for the large-aperture $L = 3$ mm grating is lower than the value predicted by the best-fit uniform-density model.

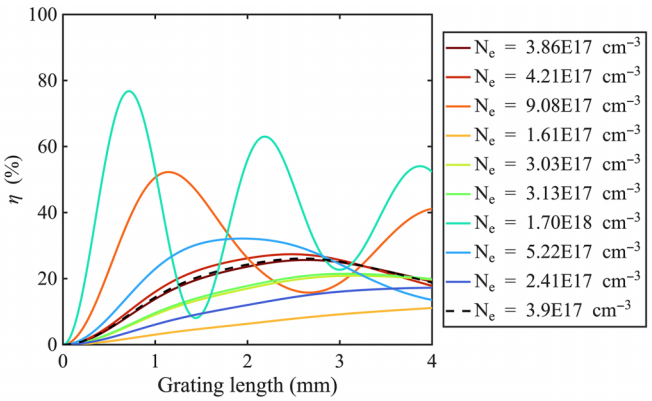


FIG. 9. Calculated diffraction efficiency as a function of grating length for each of the 9 peak electron densities at the grating fringes from Fig. 8. The black dashed line indicates the best-fit curve for the average experimental electron density of 4.9×10^{17} cm^{-3}.

In the actual grating, the signal beam propagates through multiple fringes with different electron densities as it traverses the grating. Consequently, the diffracted signal is determined by the cumulative effect of the spatially varying plasma density rather than by the efficiency of any single idealized fringe. Thus, the reduced diffraction efficiency calculated for the range of fringe densities provides a plausible explanation for the lower efficiency observed in the large-aperture configuration compared with the idealized uniform-density model.

[1] A. S. Pirozhkov, Y. Fukuda, M. Nishiuchi, H. Kiriyama, A. Sagisaka, K. Ogura, M. Mori, M. Kishimoto, H. Sakaki, N. P. Dover, K. Kondo, N. Nakanii, K. Huang, M. Kanasaki, K. Kondo, and M. Kando, Approaching the diffraction-limited, bandwidth-limited petawatt, Opt. Express **25**, 20486 (2017).

[2] Y. Wang, S. Wang, A. Rockwood, B. M. Luther, R. Hollinger, A. Curtis, C. Calvi, C. S. Menoni, and J. J. Rocca, 0.85 PW laser operation at 33 Hz and high-contrast ultrahigh-intensity $\lambda = 400$ nm second-harmonic beamline, Opt. Lett. **42**, 3828 (2017).

[3] Z. Guo, L. Yu, J. Wang, C. Wang, Y. Liu, Z. Gan, W. Li, Y. Leng, X. Liang, and R. Li, Improvement of the focusing ability by double deformable mirrors for 10 PW-level Ti:Sapphire chirped pulse amplification laser system, Opt. Express **26**, 26776 (2018).

[4] S. Gales *et al.*, The extreme light infrastructure—nuclear physics (ELI-NP) facility: New horizons in physics with 10 PW ultra-intense lasers and 20 MeV brilliant gamma beams, Rep. Prog. Phys. **81**, 094301 (2018).

[5] J. Bromage, S.-W. Bahk, I. A. Begishev, C. Dorrer, M. J. Guardalben, B. N. Hoffman, J. B. Oliver, R. G. Roides, E. M. Schiesser, M. J. Shoup III, M. Spilatro, B. Webb, D. Weiner, and J. D. Zuegel, Technology development for ultraintense all-OPCPA systems, High Power Laser Sci. Eng. **7** (2019).

[6] J. W. Yoon, Y. G. Kim, I. W. Choi, J. H. Sung, H. W. Lee, S. K. Lee, and C. H. Nam, Realization of laser intensity over 10^{23} W/cm^2, Optica **8**, 630 (2021).

[7] L. Veisz, P. Fischer, S. Vardast, F. Schnur, A. Muschet, A. De Andres, S. Kaniyeri, H. Li, R. Salh, K. Ferencz, G. N. Nagy, and S. Kahaly, Waveform-controlled field synthesis of sub-two-cycle pulses at the 100 TW peak power level, Nat. Photonics **19**, 1013 (2025).

[8] A. Maksimchuk, J. Nees, B. Hou, R. Anthony, J. Bae, F. Bayer, M. Burger, P. Campbell, J. Cardarelli, V. Contreras *et al.*, The ZEUS multi-petawatt laser system, Phys. Plasmas **32**, 103107 (2025).

[9] H. Abu-Shawareb, R. Acree, P. Adams, J. Adams, B. Addis, R. Aden, P. Adrian, B. Afeyan, M. Aggleton *et al.*,

Achievement of target gain larger than unity in an inertial fusion experiment, Phys. Rev. Lett. **132**, 065102 (2024).
[10] E. E. Los, E. Gerstmayr, C. Arran, M. J. Streeter, C. Colgan, C. C. Cobo, B. Kettle, T. G. Blackburn, N. Bourgeois, L. Calvin *et al.*, Observation of quantum effects on radiation reaction in strong fields, Nat. Commun. **17**, 1157 (2026).
[11] A. Di Piazza, C. Müller, K. Z. Hatsagortsyan, and C. H. Keitel, Extremely high-intensity laser interactions with fundamental quantum systems, Rev. Mod. Phys. **84**, 1177 (2012).
[12] V. Dewan, A. M. Zheltikov, and J. M. Mikhailova, Attosecond nonlinear quantum electrodynamics in laser-driven plasmas via two-photon synchrotron emission, Phys. Rev. Res. **8**, 033249 (2026).
[13] A. M. Zheltikov, Criteria for stochastic self-focusing, Phys. Rev. A **110**, 023516 (2024).
[14] A. M. Zheltikov, Wait time to stochastic self-focusing, Phys. Lett. A **505**, 129432 (2024).
[15] J. M. Mikhailova, Plasma optics for ultrafast high-intensity light sources, in *Proc. SPIE 13538, Coherent and Incoherent Radiation Sources based on Laser-driven Relativistic Plasma Waves, 135380E* (SPIE, 2025), 10.1117/12.3065349.
[16] M. R. Edwards, N. J. Fisch, and J. M. Mikhailova, Laser-driven plasma sources of intense, ultrafast, and coherent radiation, Phys. Plasmas **28**, 013105 (2021).
[17] M. N. Polyanskiy, I. V. Pogorelsky, M. Babzien, and M. A. Palmer, Demonstration of a 2 ps, 5 TW peak power, long-wave infrared laser based on chirped-pulse amplification with mixed-isotope CO_2 amplifiers, OSA Continuum **3**, 459 (2020).
[18] M. R. Edwards, N. M. Fasano, T. Bennett, A. Griffith, N. Turley, B. M. O'Brien, and J. M. Mikhailova, A multi-terawatt two-color beam for high-power field-controlled nonlinear optics, Opt. Lett. **45**, 6542 (2020).
[19] M. R. Edwards, J. M. Mikhailova, and N. J. Fisch, X-ray amplification by stimulated Brillouin scattering, Phys. Rev. E **96**, 023209 (2017).
[20] J. Branlard, G. Ayvazyan, V. Ayvazyan, M. Grecki, M. Hoffmann, T. Jezynski, I. Kudla, T. Lamb, F. Ludwig, U. Mavric *et al.*, The european XFEL LL RF system, IPAC **12**, 55 (2012).
[21] A. Brachmann*et al.*, Commissioning of LCLS-II, Proc. LINAC2024 (2023), pp. 589–592,
[22] N. M. Fasano, Harmonic generation in reflection from plasma mirrors, Ph.D. thesis, Princeton University, 2023, Available at http://arks.princeton.edu/ark:/88435/dsp01rn3014630.
[23] J. M. Mikhailova, A. Buck, A. Borot, K. Schmid, C. Sears, G. D. Tsakiris, F. Krausz, and L. Veisz, Ultra-high-contrast few-cycle pulses for multipetawatt-class laser technology, Opt. Lett. **36**, 3145 (2011).
[24] M. R. Edwards, N. M. Fasano, A. M. Giakas, M. M. Wang, J. Griff-McMahon, A. Morozov, V. M. Perez-Ramirez, N. Lemos, P. Michel, and J. M. Mikhailova, Greater than five-order-of-magnitude postcompression temporal contrast improvement with an ionization plasma grating, Phys. Rev. Lett. **133**, 155101 (2024).
[25] C. Thaury, F. Quere, J.-P. Geindre, A. Levy, T. Ceccotti, P. Monot, M. Bougeard, F. Réau, P. d'Oliveira, P. Audebert *et al.*, Plasma mirrors for ultrahigh-intensity optics, Nat. Phys. **3**, 424 (2007).
[26] P. Heissler, R. Hörlein, J. M. Mikhailova, L. Waldecker, P. Tzallas, A. Buck, K. Schmid, C. Sears, F. Krausz, L. Veisz *et al.*, Few-cycle driven relativistically oscillating plasma mirrors: A source of intense isolated attosecond pulses, Phys. Rev. Lett. **108**, 235003 (2012).
[27] J. M. Mikhailova, M. V. Fedorov, N. Karpowicz, P. Gibbon, V. T. Platonenko, A. M. Zheltikov, and F. Krausz, Isolated attosecond pulses from laser-driven synchrotron radiation, Phys. Rev. Lett. **109**, 245005 (2012).
[28] M. R. Edwards, V. T. Platonenko, and J. M. Mikhailova, Enhanced attosecond bursts of relativistic high-order harmonics driven by two-color fields, Opt. Lett. **39**, 6823 (2014).
[29] M. R. Edwards and J. M. Mikhailova, Waveform-controlled relativistic high-order-harmonic generation, Phys. Rev. Lett. **117**, 10 (2016).
[30] M. R. Edwards and J. M. Mikhailova, The x-ray emission effectiveness of plasma mirrors: Reexamining power-law scaling for relativistic high-order harmonic generation, Sci. Rep. **10**, 5154 (2020).
[31] N. M. Fasano, V. Dewan, M. R. Edwards, A. Giakas, T. Bennett, and J. M. Mikhailova, Cascaded plasma mirrors for two-color-driven harmonic generation, in *2024 Conference on Lasers and Electro-Optics (CLEO)* (IEEE, New York, 2024), pp. 1–2.
[32] N. Fasano, V. Dewan, and J. Mikhailova, Plasma mirrors for generating co-and counter-rotating harmonics, in *2024 Conference on Lasers and Electro-Optics (CLEO)* (IEEE, New York, 2024), pp. 1–2.
[33] S. Haessler, M. Ouillé, J. Kaur, M. Bocoum, F. Böhle, D. Levy, L. Daniault, A. Vernier, J. Faure, and R. Lopez-Martens, High-harmonic generation and correlated electron emission from relativistic plasma mirrors at 1 kHz repetition rate, Ultrafast Sci. **10**, 5154 (2022).
[34] O. Jahn, V. E. Leshchenko, P. Tzallas, A. Kessel, M. Krüger, A. Münzer, S. A. Trushin, G. D. Tsakiris, S. Kahaly, D. Kormin, L. Veisz, V. Pervak, F. Krausz, Z. Major, and S. Karsch, Towards intense isolated attosecond pulses from relativistic surface high harmonics, Optica **6**, 280 (2019).
[35] L. Chopineau, G. Blaclard, A. Denoeud, H. Vincenti, F. Quéré, and S. Haessler, Sub-laser-cycle control of relativistic plasma mirrors, Phys. Rev. Res. **4**, L012030 (2022).
[36] M. Ouillé, J. Kaur, Z. Cheng, S. Haessler, and R. Lopez-Martens, Lightwave-controlled relativistic plasma mirrors, Opt. Lett. **49**, 4847 (2024).
[37] N. M. Fasano, M. R. Edwards, and J. M. Mikhailova, Electron bunch dynamics and emission in particle-in-cell simulations of relativistic laser–solid interactions: On density artifacts, collisions, and numerical dispersion, Phys. Plasmas **30**, 063904 (2023).
[38] M. R. Edwards, N. M. Fasano, and J. M. Mikhailova, Electron-nanobunch-width-dominated spectral power law for relativistic harmonic generation from ultrathin foils, Phys. Rev. Lett. **124**, 185004 (2020).
[39] M. R. Edwards and J. M. Mikhailova, Multipass relativistic high-order-harmonic generation for intense attosecond pulses, Phys. Rev. A **93**, 023836 (2016).
[40] V. E. Leshchenko, A. Kessel, O. Jahn, M. Krüger, A. Münzer, S. A. Trushin, L. Veisz, Z. Major, and S. Karsch, On-target temporal characterization of optical pulses at relativistic intensity, Light:Sci. Appl. **8**, 96 (2019).

[41] P. Michel, L. Divol, D. Turnbull, and J. D. Moody, Dynamic control of the polarization of intense laser beams via optical wave mixing in plasmas, Phys. Rev. Lett. **113**, 205001 (2014).
[42] K. Qu, Q. Jia, and N. J. Fisch, Plasma q-plate for generation and manipulation of intense optical vortices, Phys. Rev. E **96**, 053207 (2017).
[43] A. Morozov, A. Goltsov, Q. Chen, M. Scully, and S. Suckewer, Ionization assisted self-guiding of femtosecond laser pulses, Phys. Plasmas **25**, 053110 (2018).
[44] L. Feder, B. Miao, J. E. Shrock, A. Goffin, and H. M. Milchberg, Self-waveguiding of relativistic laser pulses in neutral gas channels, Phys. Rev. Res. **2**, 043173 (2020).
[45] N. Lemos, L. Cardoso, J. Geada, G. Figueira, F. Albert, and J. Dias, Guiding of laser pulses in plasma waveguides created by linearly-polarized femtosecond laser pulses, Sci. Rep. **8**, 3165 (2018).
[46] A. Picksley, J. Stackhouse, C. Benedetti, K. Nakamura, H. Tsai, R. Li, B. Miao, J. Shrock, E. Rockafellow, H. Milchberg *et al.*, Matched guiding and controlled injection in dark-current-free, 10-GeV-class, channel-guided laser-plasma accelerators, Phys. Rev. Lett. **133**, 255001 (2024).
[47] R. Rankin, N. H. Burnett, P. B. Corkum, and C. E. Capjack, Refraction effects associated with multiphoton ionization and ultrashort-pulse laser propagation in plasma waveguides, Opt. Lett. **16**, 835 (1991).
[48] H.-C. Wu, Z.-M. Sheng, Q.-J. Zhang, Y. Cang, and J. Zhang, Manipulating ultrashort intense laser pulses by plasma Bragg gratings, Phys. Plasmas **12**, 113103 (2005).
[49] M. R. Edwards and P. Michel, Plasma transmission gratings for compression of high-intensity laser pulses, Phys. Rev. Appl. **18**, 024026 (2022).
[50] G. Lehmann and K. H. Spatschek, Plasma-grating-based laser pulse compressor, Phys. Rev. E **110**, 015209 (2024).
[51] M. M. Wang, V. M. Perez-Ramirez, A. Das, I. Tigges-Green, V. Dewan, K. Ou, S. Cao, P. Michel, M. R. Edwards, and J. M. Mikhailova, Experimental demonstration of chromatic angular dispersion from transmission plasma gratings, in *2025 Conference on Lasers and Electro-Optics (CLEO)* (IEEE, New York, 2025), pp. 1–2.
[52] V. M. Perez-Ramirez, M. M. Wang, K. Ou, S. Cao, D. Singh, N. M. Fasano, V. Dewan, A. M. Giakas, A. Das, I. Tigges-Green, P. Michel, J. M. Mikhailova, and M. R. Edwards, Dispersive properties of plasma diffraction gratings: Towards plasma-based laser pulse compression, arXiv:2604.27165.
[53] J. P. Palastro, D. Gordon, B. Hafizi, L. A. Johnson, J. Peñano, R. F. Hubbard, M. Helle, and D. Kaganovich, Plasma lenses for ultrashort multi-petawatt laser pulses, Phys. Plasmas **22**, 123101 (2015).
[54] M. R. Edwards, V. R. Munirov, A. Singh, N. M. Fasano, E. Kur, N. Lemos, J. M. Mikhailova, J. S. Wurtele, and P. Michel, Holographic plasma lenses, Phys. Rev. Lett. **128**, 065003 (2022).
[55] Z.-M. Sheng, J. Zhang, and D. Umstadter, Plasma density gratings induced by intersecting laser pulses in underdense plasmas, Appl. Phys. B **77**, 673 (2003).
[56] G. Lehmann and K. H. Spatschek, Transient plasma photonic crystals for high-power lasers, Phys. Rev. Lett. **116**, 225002 (2016).
[57] M. Durand, A. Jarnac, Y. Liu, B. Prade, A. Houard, V. Tikhonchuk, and A. Mysyrowicz, Dynamics of plasma gratings in atomic and molecular gases, Phys. Rev. E **86**, 036405 (2012).
[58] L. Shi, W. Li, Y. Wang, X. Lu, L. Ding, and H. Zeng, Generation of high-density electrons based on plasma grating induced Bragg diffraction in air, Phys. Rev. Lett. **107**, 095004 (2011).
[59] C. Zhang, Z. Nie, Y. Wu, M. Sinclair, C.-K. Huang, K. A. Marsh, and C. Joshi, Ionization induced plasma grating and its applications in strong-field ionization measurements, Plasma Phys. Controlled Fusion **63**, 095011 (2021).
[60] J. Liu, W. Li, H. Pan, and H. Zeng, Two-dimensional plasma grating by non-collinear femtosecond filament interaction in air, Appl. Phys. Lett. **99**, 151105 (2011).
[61] S. Suntsov, D. Abdollahpour, D. G. Papazoglou, and S. Tzortzakis, Femtosecond laser induced plasma diffraction gratings in air as photonic devices for high intensity laser applications, Appl. Phys. Lett. **94**, 251104 (2009).
[62] M. G. Moharam and L. Young, Criterion for Bragg and Raman-Nath diffraction regimes, Appl. Opt. **17**, 1757 (1978).
[63] M. R. Edwards, S. Waczynski, E. Rockafellow, L. Manzo, A. Zingale, P. Michel, and H. M. Milchberg, Control of intense light with avalanche-ionization plasma gratings, Optica **10**, 1587 (2023).
[64] M. Takeda, H. Ina, and S. Kobayashi, Fourier-transform method of fringe-pattern analysis for computer-based topography and interferometry, J. Opt. Soc. Am. **72**, 156 (1982).
[65] P. Yeh and W. Moerner, Introduction to photorefractive nonlinear optics (1994).
[66] A. Jarnac, M. Durand, Y. Liu, B. Prade, A. Houard, V. Tikhonchuk, and A. Mysyrowicz, Study of laser induced plasma grating dynamics in gases, Opt. Commun. **312**, 35 (2014).
[67] M. V. Ammosov, N. B. Delone, and V. P. Krainov, Tunnel ionization of complex atoms and of atomic ions in an alternating electromagnetic field, Sov. Phys. JETP, **64**, 1191 (1986).
[68] M. M. Wang, V. M. Perez-Ramirez, N. M. Fasano, K. Ou, S. Cao, V. Dewan, A. M. Giakas, A. Morozov, P. Michel, M. R. Edwards, and J. M. Mikhailova, Experimental and theoretical data (2026), https://drive.google.com/drive/folders/1DYy55fyrnJdBUXTl62qMd2k1aFGxB389.